Ab initio study of hot electrons in GaAs

Marco Bernardi[a,b], Derek Vigil-Fowler[a,b], Chin Shen Ong[a], Jeffrey B. Neaton[a,b,c,d], and Steven G. Louie[a,b,1]

[a]Department of Physics, University of California, Berkeley, CA 94720; [b]Materials Science Division and [c]Molecular Foundry, Lawrence Berkeley National Laboratory, Berkeley, CA 94720; and [d]Kavli Institute for Energy Nanosciences, Department of Physics, University of California, Berkeley, CA 94720

Edited by Allan H. MacDonald, The University of Texas at Austin, Austin, TX, and approved March 16, 2015 (received for review October 9, 2014)

Hot carrier dynamics critically impacts the performance of electronic, optoelectronic, photovoltaic, and plasmonic devices. Hot carriers lose energy over nanometer lengths and picosecond timescales and thus are challenging to study experimentally, whereas calculations of hot carrier dynamics are cumbersome and dominated by empirical approaches. In this work, we present ab initio calculations of hot electrons in gallium arsenide (GaAs) using density functional theory and many-body perturbation theory. Our computed electron–phonon relaxation times at the onset of the Γ, L, and X valleys are in excellent agreement with ultrafast optical experiments and show that the ultrafast (tens of femtoseconds) hot electron decay times observed experimentally arise from electron–phonon scattering. This result is an important advance to resolve a controversy on hot electron cooling in GaAs. We further find that, contrary to common notions, all optical and acoustic modes contribute substantially to electron–phonon scattering, with a dominant contribution from transverse acoustic modes. This work provides definitive microscopic insight into hot electrons in GaAs and enables accurate ab initio computation of hot carriers in advanced materials.

hot carriers | semiconductors | GaAs | ultrafast | electron–phonon scattering

Hot carriers (HCs) generated by the absorption of light or injection at a contact are commonly found in many advanced technologies (1–9). In electronics, the operation of high-speed devices is controlled by HC dynamics, and HC injection is a key degradation mechanism in transistors (10, 11). In solar cells and plasmonics, recent work has focused on extracting the kinetic energy of HCs before cooling (7, 9), a process defined here as the energy loss of HCs, ultimately leading to thermal equilibrium with phonons. HC dynamics is also crucial to interpret time-resolved spectroscopy experiments used to study excited states in condensed matter (12). This situation has sparked a renewed interest in HCs in a broad range of materials of technological relevance.

Experimental characterization of HCs is challenging because of the subpicosecond timescale associated with the electron–phonon (*e*-ph) and electron–electron (*e*-*e*) scattering processes regulating HC dynamics. For example, HCs can be studied using ultrafast spectroscopy, but microscopic interpretation of time-resolved spectra requires accurate theoretical models. However, modeling of HCs thus far has been dominated by empirical approaches, which do not provide atomistic details and use ad hoc parameters to fit experiments (13, 14). Notwithstanding the pioneering role of these early studies, the availability of accurate ab initio computational methods based on density functional theory (DFT) (15) and many-body perturbation theory (16) enables studies of HCs with superior accuracy, broad applicability, and no need for fitting parameters.

Hot electrons in gallium arsenide (GaAs) are of particular interest because of the high electron mobility and multivalley character of the conduction band. Electrons excited at energies greater than ∼0.5 eV above the conduction band minimum (CBM) can transfer from the Γ to the L and X valleys, with energy minima at ∼0.25 and ∼0.45 eV above the CBM, respectively (17). Such intervalley scattering processes play a crucial role in hot electron cooling and transport at high electric fields.

Ample experimental data exist on hot electron transport and cooling in GaAs (12, 18–21). The interpretation of these experiments relies on Monte Carlo simulations using multiple parameters fit to experimental results. For example, Fischetti and Laux (13) used two empirical deformation potentials to model electron scattering induced by optical and acoustic phonons. Additionally, Fischetti and Laux (13) used simplified band structure and phonon dispersions. We note that, because multiple parameter sets can fit experimental results, the HC scattering rates due to different physical processes obtained empirically are not uniquely determined (13, 14).

Although heuristic approaches can provide some insight into HC dynamics of well-characterized materials (e.g., GaAs), there is a lack of generally applicable, predictive, and parameter-free approaches to study HCs.

Here, we carry out ab initio calculations of hot electrons in GaAs with energies up to 5 eV above the CBM. Our ability to use extremely fine grids in the Brillouin zone (BZ) allows us to resolve hot electron scattering in the conduction band with unprecedented accuracy. We focus here on three main findings. First, our overall computed *e*-ph scattering rates are in excellent agreement with those in previous semiempirical calculations in ref. 13 that combine multiple empirical parameters. The advantage of our approach is the ability to compute the electronic band and momentum dependence of the *e*-ph scattering rates without fitting parameters. Second, we show that both optical and acoustic modes contribute substantially to *e*-ph scattering, with a dominant scattering from transverse acoustic (TA) modes. This result challenges the tenet that HCs lose energy mainly through longitudinal optical (LO) phonon emission. Third, our calculations provide valuable means for quantitative interpretation of experiments of hot electron cooling in GaAs. In particular, the ultrafast (∼50 fs) *e*-ph relaxation times that we compute at the onset of the X valley are in excellent agreement with the fastest decay time observed in ultrafast optical experiments (18, 19, 21). This signal was attributed by some (18) to *e*-*e* scattering and by others (21) to *e*-ph scattering. The excellent agreement with time decay signals in time-resolved experiments

Significance

How does an excited electron lose its energy? This problem is central in fields ranging from condensed matter physics to electrical engineering and chemistry. The cooling of hot electrons in gallium arsenide (GaAs) is the critical process underlying the operation of exciting electronic and optoelectronic devices, but the nature of this cooling is controversial. Here, we present calculations showing that hot electrons in GaAs lose energy chiefly by emitting lattice vibrations. We find a dominant role of acoustic vibrations, challenging the common notion that optical vibrations dominate excited electron energy loss. Our computational approach shines light on microscopic processes that are hard to capture with both experiments and semi-empirical calculations and opens new avenues to compute excited electron dynamics.

Author contributions: M.B., D.V.-F., J.B.N., and S.G.L. designed research; M.B., D.V.-F., and C.S.O. performed calculations; M.B., D.V.-F., J.B.N., and S.G.L. analyzed data; M.B., D.V.-F., J.B.N., and S.G.L. wrote the paper; and C.S.O. contributed to code development.

The authors declare no conflict of interest.

This article is a PNAS Direct Submission.

[1]To whom correspondence should be addressed. Email: sglouie@berkeley.edu.

This article contains supporting information online at www.pnas.org/lookup/suppl/doi:10.1073/pnas.1419446112/-/DCSupplemental.

shows the dominant role of *e*-ph scattering for hot electron cooling at low carrier density.

Our approach combines electronic band structures computed ab initio using the *GW* (where *G* is the Green function, *W* is the screened Coulomb potential, and *GW* is the diagram employed for the electron exchange-correlation interactions) method (16) with phonon dispersions from density functional perturbation theory (DFPT) (22), and it is entirely free of empirical parameters. We compute the *e*-ph matrix elements using a Wannier function formalism (23) on very fine BZ grids and are able to resolve *e*-ph scattering for the different conduction band valleys. The *e*-*e* rates for hot electrons—also known as impact ionization (II) rates—are computed using the *GW* method (16, 24), and thus include dynamical screening effects. Additional details of our calculations are discussed in *Methods*.

Results and Discussion

Accurate determination of *e*-ph scattering rates is essential to understand HC cooling with microscopic detail. Fig. 1*A* shows the computed *e*-ph scattering rates for hot electrons in GaAs with energies up to 5 eV above the CBM. Throughout the manuscript, all energies are referenced to the CBM. The *e*-ph scattering rates follow trends similar to the electronic density of states (DOS), consistent with the fact that the DOS reflects the available phase space for *e*-ph scattering. At a fixed energy, the scattering rates are distributed over a range of values caused by the **k** dependence of the *e*-ph matrix elements (here, **k** is the crystal momentum of the electronic state in the BZ). We find a significant spread in the scattering rates for a fixed energy by up to ∼25% of their average value.

We carry out a quantitative analysis of the contributions from the individual phonon modes to the *e*-ph scattering rates. Analytical treatments of *e*-ph scattering in polar materials have relied extensively on the Fröhlich Hamiltonian (25–27), which couples electrons to LO phonons. This fact has often led to the assumption that *e*-ph scattering in polar materials is primarily caused by coupling of electrons with LO phonon modes. Fig. 1 *B* and *C* shows that all optical and acoustic modes contribute substantially to *e*-ph scattering in GaAs. Our calculations show that the TA modes provide the single largest contribution to *e*-ph scattering, whereas the LO modes possess the greatest scattering rates among the optical modes. The scattering rates from acoustic modes are overall roughly two times the value of the optical modes. These results highlight the limitations of previous models using LO phonon scattering alone and emphasize the need for ab initio calculations with fine **k** grids to obtain quantitative evaluations of *e*-ph scattering.

The total ab initio *e*-ph scattering rates (i.e., summed over all modes) computed here are in excellent agreement with those obtained by Fischetti and Laux (13) (Fig. 2*A*), who used empirical deformation potentials to describe the coupling to optical and acoustic modes and the Fröhlich Hamiltonian to take into account the long-range effect on electrons of the LO phonons. Their empirical approach yields *e*-ph scattering rates able to reproduce experimental velocity-field curves in Monte Carlo calculations. The agreement with the total *e*-ph scattering rates fit to experiment highlights the accuracy of our ab initio approach and validates the Monte Carlo simulations carried out in ref. 13. Clearly, the additional benefit of our approach is the ability to compute *e*-ph scattering rates in the absence of experimental data. The agreement obtained here is striking given that multiple empirical parameters were used in ref. 13. We provide a detailed analysis of this result to understand the differences between previous semiempirical *e*-ph calculations and our ab initio approach.

As noted by Ziman (27), accurate calculations of *e*-ph matrix elements are the nub of the *e*-ph interaction. For a scattering process connecting two electronic states that differ in crystal momentum by $\hbar\mathbf{q}$, the *e*-ph matrix element is an integral of the initial and final Bloch states and the change in the crystal potential caused by a phonon with wavevector **q** (Eq. **2**). Direct computation of such *e*-ph matrix elements within the adiabatic approximation requires knowledge of the potential acting on the electrons as well as the phonon eigenvectors and Bloch states in the entire BZ. Computation of these quantities has become possible owing to the advent of DFT and related methods (15), which were later extended to compute and interpolate *e*-ph matrix elements on fine reciprocal space grids (23, 28). Such detailed calculations were technically unfeasible in the early days of semiconductor physics and in particular, at the time of the work in ref. 13. The *e*-ph matrix elements were often approximated by mode-dependent parameters called deformation potentials (13, 14, 27) and multiplied by an overlap integral over the unit cell between the initial and final electronic states (13, 27). In polar materials, such as GaAs, the Fröhlich Hamiltonian (25) was added explicitly to take into account the long-range electric fields generated by LO vibrations of the ions. The deformation potentials were then tuned until agreement with carrier velocity vs. electric field or other transport data was achieved in Monte Carlo calculations using the computed *e*-ph scattering rates. However, because multiple deformation potentials are used in such semiempirical *e*-ph calculations, different choices of the parameters are able to reproduce

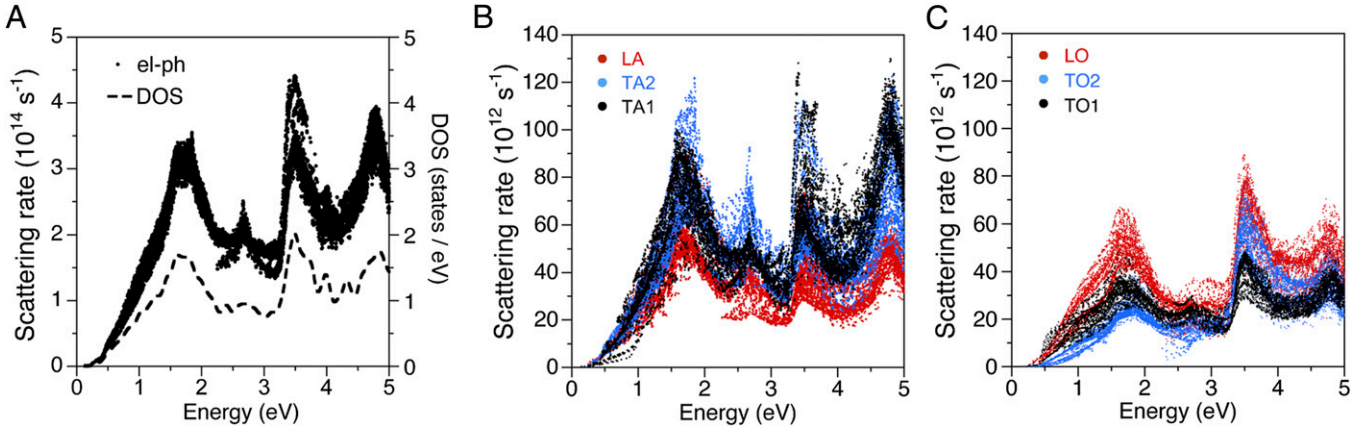

Fig. 1. *e*-ph scattering in GaAs. (*A*) *e*-ph scattering rates for hot electrons in GaAs shown together with the electronic DOS. The zero of the energy axis is the CBM. The contributions to the total *e*-ph scattering rate in *A* from the acoustic and optical phonons are shown in *B* and *C*, respectively. LA, TA, LO, and TO label *e*-ph scattering induced by LA, TA, LO, and TO phonons in *B* and *C*. The sum of the scattering rates in *B* and *C* equals the total scattering rate in *A*.

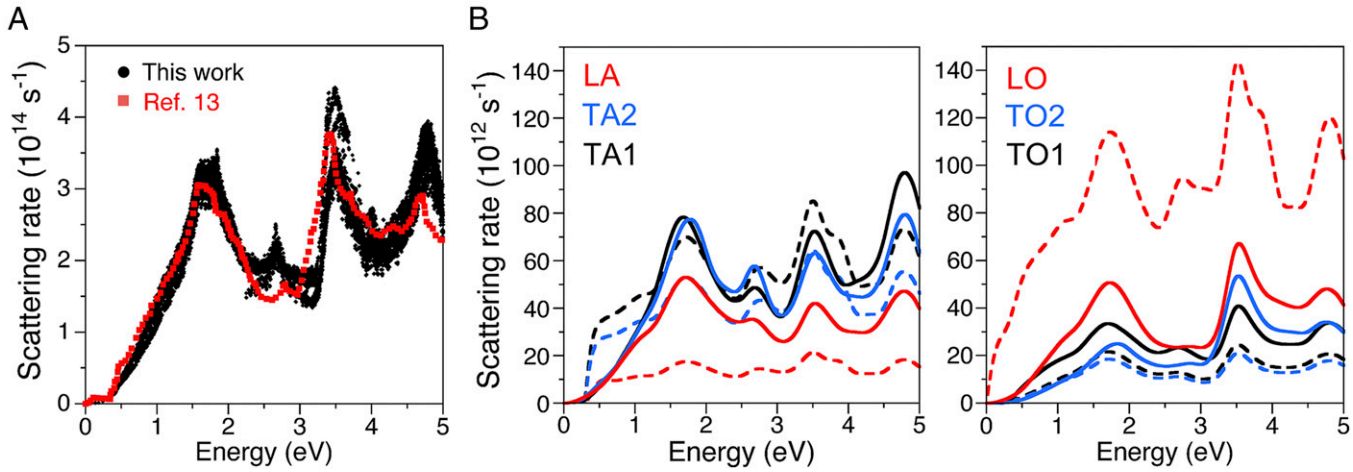

Fig. 2. Comparison of ab initio and semiempirical calculations. (*A*) e-ph scattering rates from all modes in our work vs. those in ref. 13. (*B*) Contributions of individual phonon modes to the e-ph scattering rate for ab initio calculations (solid lines) carried out in this work and semiempirical calculations (dashed lines) that we reproduce using the parameters in ref. 13. The curves shown are the **k**-averaged scattering rates for (*Left*) acoustic modes and (*Right*) optical modes.

the total *e*-ph scattering rates and thus, the experimental data. The contributions of individual phonon modes are, thus, ambiguously determined in the semiempirical approach, because they are arbitrarily set by the particular choice of the deformation potentials. In contrast, individual phonon contributions are uniquely determined in ab initio calculations.

To carry out a quantitative comparison of the individual phonon mode contributions with the work by Fischetti and Laux (13), we attempted to reproduce their calculations by combining our band structures and phonon dispersions with their deformation potential parameters (*Methods*). The total *e*-ph scattering rates obtained with this approach agree well with ref. 13, thus guaranteeing that we correctly reproduced their calculations. Fig. 2*B* shows a comparison between this work and ref. 13 of the *e*-ph scattering rates from individual phonon modes. Despite the fact that the total scattering rates are in excellent agreement, we find that the scattering rates from individual phonon modes largely differ in the two approaches. Compared with our ab initio calculations, scattering by longitudinal acoustic (LA) phonons is largely underestimated, and scattering by LO phonons is largely overestimated in ref. 13. In addition, scattering by transverse optical (TO) phonons is slightly underestimated, whereas scattering by TA phonons is adequately described in ref. 13. The too-large LO *e*-ph scattering rates in ref. 13 seem to be compensated by too-small acoustic scattering rates compared with our calculations as a consequence of the arbitrary choice of deformation potential parameters for acoustic phonons. The different LO scattering rates are caused by a key difference between the ab initio treatment of the *e*-ph interaction in polar materials and semiempirical theories. In the ab initio approach, explicit inclusion of the Fröhlich Hamiltonian becomes redundant, because it assumes the concept of rigid ions carrying a net charge. Inclusion of both Fröhlich and nonpolar matrix elements for LO phonons in semiempirical treatments is clearly ad hoc, because it arbitrarily separates the long- and short-range *e*-ph interactions, which are taken into account on the same footing in ab initio calculations. Future work will be necessary to more fully establish the differences between the ab initio approach based on DFT adopted here and semiempirical theories for a range of polar and nonpolar materials.

The main practical challenge to control HC dynamics in devices is the subpicosecond timescale for HC cooling. This situation has led to extensive studies with ultrafast pump-probe spectroscopies to understand the microscopic details of HC cooling. Fig. 3*A* shows our computed *e*-ph relaxation times (defined here as the inverses of the *e*-ph scattering rates) for energies up to 1.5 eV. We find relaxation times of ~1.5 ps, 200 fs, and 50 fs at energies near the bottom of the Γ, L, and X valleys, respectively. Within an

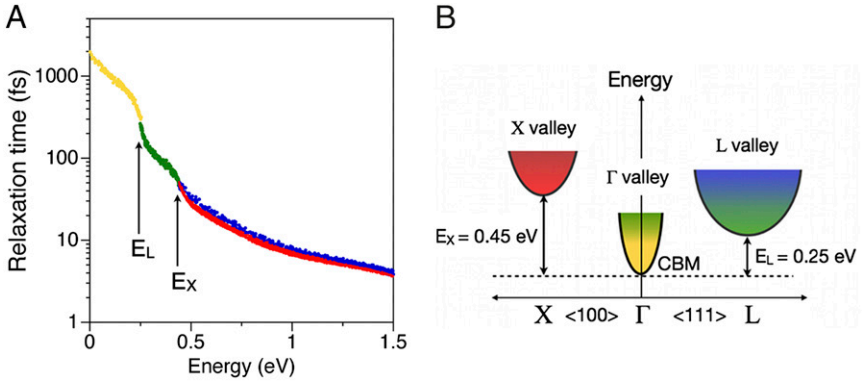

Fig. 3. *e*-ph relaxation times in GaAs. (*A*) *e*-ph relaxation times of hot electrons in GaAs. Up to E_X, data points shown in yellow originate from electronic states in the Γ valley, and data points shown in green originate from states at the bottom of the L valley. At energies above E_X, states in red and blue are located near the X and L valleys, respectively. (*B*) Schematic of the states and valleys giving rise to the *e*-ph scattering rates in *A*.

optical phonon energy (~40 meV in GaAs) of the onset energy of the valleys, the *e*-ph relaxation times increase rapidly as the carrier energy approaches the valley minima because of the decrease in the DOS of the given valley and the resulting decrease in the phase space for intravalley *e*-ph scattering.

The energy range above E_X has been studied extensively in ultrafast optical experiments because of the coexistence of the Γ, L, and X valleys. We find that the relaxation times decrease rapidly from ~200 fs at E_L to ~10 fs at 1.5 eV energy and remain nearly constant above 1.5 eV. At the onset of the X valley at energy E_X, the scattering rates split into two different curves, with one set of scattering rates higher than the other by ~10%. The higher scattering rates are associated with hot electron states in the X valleys, whereas the lower scattering rates stem from hot electrons in the L valleys. The distinct behavior of the two sets of states extends up to 1.5 eV and thus, for ~1 eV above E_X. We remark that existing models of *e*-ph scattering in GaAs have so far relied on energy- but not **k**-dependent scattering rates. Our calculations show that the scattering rates for the L and X valleys are slightly different, thus complicating the hot electron dynamics caused by intervalley scattering.

Below, we use our calculations to analyze previous experiments of hot electron cooling after excitation with ~2 eV light (18–21). These experiments use time-resolved absorption and luminescence measurements with sub-100–fs time resolutions and report inelastic scattering of the hot electrons over tens of femtoseconds. Such ultrafast inelastic processes were attributed by some to *e-e* scattering (18), even at low carrier density, where *e-e* scattering is typically minimal (12). Other works attributed the fast inelastic scattering to *e*-ph processes. For example, Young et al. (21) have carried out transient absorption experiments at different carrier densities and found that the decay of the absorption bleaching signal shows little variation with carrier density. At low carrier density, where *e*-ph is typically the dominant inelastic scattering process, Young et al. (21) find that the recovery of the bleaching at 2 eV can be fit by three exponentials with decay times of 35 fs, 185 fs, and 1.4 ps and attribute these features to *e*-ph scattering. We find that the decay times in the work in ref. 21 are in excellent agreement with the relaxation times presented in Fig. 3*A*, which are discussed next.

The valence band edge of GaAs is split at Γ because of the spin–orbit interaction into two valence band maximum (VBM) states (heavy- and light-hole bands) and the split-off (SO) band located 350 meV below the VBM. Given the ~1.4-eV gap of GaAs, pumping with 2 eV light, thus, generates hot electron populations at energies of ~0.5 eV above the CBM because of excitation from the heavy- and light-hole bands and ~0.15 eV because of excitation from the SO band (21). Our computed *e*-ph relaxation time of ~50 fs at 0.5 eV above the CBM is in very good agreement with the 35-fs decay signal found experimentally by Young et al. (21) and attributed to intervalley scattering from the Γ to the L and X valleys. In addition, the 185-fs timescale attributed in ref. 21 to *e*-ph scattering of electrons excited from the SO band agrees well with the ~200-fs relaxation time that we predict at the bottom of the L valley. Finally, the 1.4-ps rate for the overall carrier cooling is in agreement with a fast transfer to the Γ valley followed by cooling to the CBM with ~1.5-ps relaxation time as found in our calculations.

In comparing experimental decay times of the bleaching signal with computed *e*-ph relaxation times, one must keep in mind that the pump pulse has a finite energy resolution and thus, generates a pocket of carriers with a spread in energy. The probe pulse also has a finite energy resolution and captures average carrier relaxation times from several states. Given these differences and considering the rapid variation of the computed *e*-ph scattering rates around E_L, we believe that the attribution in ref. 21 of the 185-fs decay signal to the electrons excited from the SO band is correct and consistent with our calculation. Although a direct comparison of state-specific *e*-ph relaxation times (i.e., state lifetimes) with decay times in transient absorption experiments is approximate, we believe it is justified here by the fact that the probe populates well-defined conduction band states; therefore, the bleaching decay time in ref. 21 can be interpreted as the relaxation time or state lifetime of specific conduction band states, consistent with the interpretation given in ref. 21. Our data seem to confirm the interpretation in ref. 21 that the *e*-ph interaction alone can account for the ultrafast inelastic scattering at low carrier density observed in several experiments (18–21).

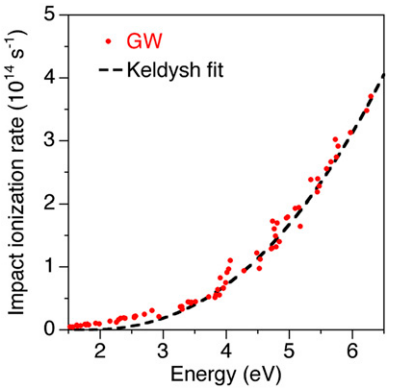

Fig. 4. II rates in GaAs. II rates computed with the *GW* method shown together with the Keldysh fit. The energies are referenced to the CBM and extend to ~5 eV above the II threshold.

To further show that *e*-ph scattering dominates the cooling of low-energy hot electrons, we carry out *GW* calculations of the II rates (*Methods*), which are shown in Fig. 4. The II rates are well-fit by a Keldysh formula: $\Gamma_{II} = \alpha \cdot (E - E_{th})^{\beta}$, where Γ_{II} is the II rate, E_{th} is a threshold energy for the onset of II, and α and β are fitting coefficients. Similar to previous work (13, 29, 30), we use a threshold $E_{th} = 1.7$ eV for the onset of II and obtain fitting coefficients of $\alpha = 10^{13}$ s^{-1} and $\beta = 2.36$. The threshold is numerically close to the *GW* band gap of GaAs, and the value of β deviates from the parabolic trend (i.e., $\beta = 2$) found in the free electron gas (26) caused by the multiband character of GaAs. The II rates become greater than the *e*-ph rates at energy higher than ~6 eV, and we, thus, predict that energy loss for hot electrons with energy higher than 6 eV is dominated by inelastic II and Auger processes. Because of the use of the random phase approximation (RPA) screening in the *GW* formalism, our approach can provide accurate rates for interband II processes induced by the screened Coulomb interaction. However, phonon-assisted II processes are not included in the *GW* formalism and may result in underestimating the experimental II rates.

In assessing the accuracy of our calculations, we note that recent ab initio calculations of Auger scattering (i.e., the inverse process of II) show that phonon-assisted Auger rates are at least one order of magnitude higher than the Auger rates caused by the Coulomb interaction alone (31). This finding suggests that accurate calculations of II rates caused by the Coulomb interaction should underestimate the experimental II rates caused by the absence of phonon-assisted processes. The empirical II rates calculations in ref. 13 should be able to yield the correct order of magnitude for the II rates because of their accurate *e*-ph rates and the fit to experiment data. The absence of phonon-assisted processes in our approach justifies our lower II rates compared with those in ref. 13 (Fig. S1). However, even with the II rates in ref. 13, our conclusions are unchanged regarding the dominant role of the *e*-ph scattering for hot electron cooling up to ~2 eV energy as used in the experiments considered here.

Finally, we note that our *e-e* scattering rates do not include *e-e* scattering among excited carriers within the conduction band,

namely processes whereby a hot electron loses energy by transferring it to another conduction band electron. At high carrier density (e.g., greater than 10^{18} cm^{-3}), this mechanism is important to achieve equilibrium within the hot electron gas, because it leads to the establishment of a hot electron temperature and a corresponding HC Fermi–Dirac distribution. Our scattering rates are, thus, expected to be accurate only at relatively low carrier density. We note that at high carrier density the *GW* formalism can, in principle, account for *e*-*e* scattering within the conduction band provided that the dielectric screening and Green functions are appropriately computed with an additional assumed out-of-equilibrium initial carrier distribution or alternatively, a hot Fermi–Dirac distribution. However, one problem associated with this approach is that such *e*-*e* scattering processes are so fast that they usually take place while the pump pulse is still on; therefore, an initial carrier distribution cannot be defined for the computation of the *GW* self-energy. To circumvent this bottleneck, truly nonequilibrium ab initio theories need to be developed [for example, by evolving in time nonequilibrium Green's functions on the Keldysh contour (32)], which is beyond the scope of this study.

Conclusion

In summary, although the theoretical interpretation of HC dynamics and time-resolved spectroscopy without empirical parameters is still in its infancy, our ab initio calculations show excellent agreement with semiempirical *e*-ph scattering rates and ultrafast spectroscopy data. Taken together, these results show the dominant role of *e*-ph scattering in hot electron cooling in GaAs. Our work further highlights the need to treat *e*-ph interactions in GaAs (and more broadly, polar semiconductors) with models going beyond the Fröhlich Hamiltonian and include all phonon modes on the same footing with ab initio calculations of *e*-ph scattering. Although such calculations are currently computationally expensive and highly specialized, our recent improvements in the algorithms (to be reported in the future) can make them more broadly accessible. The computational approach to study HCs and ultrafast electron scattering shown in this work is general and can be applied to semiconductors, insulators, metals, surfaces, and nanostructures. HCs are relevant in several branches of materials science and applied physics, including electronics, optoelectronics, semiconductor physics, solar energy, plasmonics, and spectroscopy. In several cases of practical interest (e.g., solar energy conversion, plasmonics, and photocatalysis), HCs are generated at low density, and therefore, the approach developed here can capture HC cooling processes of relevance in these applications.

Methods

We carry out ab initio calculations on GaAs in the diamond structure with a DFT-relaxed lattice parameter of 5.55 Å. The ground-state electronic structure is computed within the local density approximation (LDA) of DFT using the QUANTUM ESPRESSO code (33–35). Norm-conserving pseudopotentials are used to describe the core–valence interaction (36), and a kinetic energy cutoff of 45 Ry is used for the plane-wave basis set; *e*-ph and II calculations are discussed below.

***e*-ph Scattering Calculations.** Lattice dynamical properties are computed by means of DFPT (22). We use an in-house modified version of the EPW code (28) to compute the imaginary part of the lowest order *e*-ph self-energy, $\mathrm{Im}(\Sigma^{e-ph}_{n,\mathbf{k}})$, for the Bloch state of energy $\epsilon_{n,\mathbf{k}}$ at band n and $\mathbf{k}$ point in the BZ:

$$\mathrm{Im}\,\Sigma^{e-ph}_{n\mathbf{k}} = \sum_{m,\lambda,\mathbf{q}} \left|g^{\lambda,\mathbf{q}}_{n,m,\mathbf{k}}\right|^2 \mathrm{Im}\left[\frac{N_{\lambda,\mathbf{q}}+1-f_{m,\mathbf{k}}}{\epsilon_{n,\mathbf{k}}-\epsilon_{m,\mathbf{k}+\mathbf{q}}-\hbar\omega_{\lambda,\mathbf{q}}-i\eta} + \frac{N_{\lambda,\mathbf{q}}+f_{m,\mathbf{k}}}{\epsilon_{n,\mathbf{k}}-\epsilon_{m,\mathbf{k}+\mathbf{q}}+\hbar\omega_{\lambda,\mathbf{q}}-i\eta}\right], \quad [1]$$

where $\epsilon_{n,\mathbf{k}}$ is the *GW* quasiparticle energy, $\hbar\omega_{\lambda,\mathbf{q}}$ is the energy of a phonon with polarization λ and wavevector $\mathbf{q}$ in the BZ, $f_{m,\mathbf{k}}$ and $N_{\lambda,\mathbf{q}}$ are Fermi and Bose occupation numbers, respectively (evaluated here at room temperature), and η is a small Lorentzian broadening (here, we use η = 10 meV). In Eq. **1**, the key quantities are the *e*-ph matrix elements, which are defined as

$$g^{\lambda,\mathbf{q}}_{n,m,\mathbf{k}} = \sqrt{\hbar/(2M\omega_{\lambda,\mathbf{q}})}\langle\Psi_{m,\mathbf{k}+\mathbf{q}}|\partial_{\lambda,\mathbf{q}}V|\Psi_{n,\mathbf{k}}\rangle, \quad [2]$$

where $\Psi_{n,\mathbf{k}}$ is the Kohn–Sham wave function for band n and $\mathbf{k}$ in the BZ, $\partial_{\lambda,\mathbf{q}}V$ is the variation of the Kohn–Sham potential for a unit displacement of the nuclei along the phonon mode of polarization λ and wavevector $\mathbf{q}$, and M is the mass of the unit cell. The *e*-ph scattering rate $I^{e-ph}_{n,\mathbf{k}}$ is computed from the imaginary part of the self-energy as $I^{e-ph}_{n,\mathbf{k}} = (2/\hbar)\cdot\mathrm{Im}(\Sigma^{e-ph}_{n,\mathbf{k}})$, and the relaxation time $\tau_{n,\mathbf{k}} = (I^{e-ph}_{n,\mathbf{k}})^{-1}$ is the inverse of the scattering rate. We remark that this procedure is equivalent to applying perturbation theory in the lowest order of the *e*-ph perturbation (26). We first compute the electronic states on an $8\times8\times8$ **k**-point grid using DFT corrected with the *GW* self energies and the vibrational states on an $8\times8\times8$ **q**-point grid using DFPT. The *e*-ph matrix elements are computed using these coarse grids. We then interpolate the quantities needed to evaluate the *e*-ph self-energy on significantly finer grids using an interpolation procedure based on Wannier functions implemented in the EPW code (28). Our fine grids consist in a $40\times40\times40$ **k**-point grid and up to 512,000 random **q** points in the BZ. Such fine grids allow us to fully converge the self-energy in Eq. **1**. The scattering rates for the individual phonon modes shown in Fig. 1 are computed by restricting the summation in Eq. **1** to a given phonon mode (i.e., a given phonon branch and thus, a given value of λ). The *e*-ph relaxation times near the bottom of the valleys in Fig. 3 were computed separately with fine grids up to $200\times200\times200$ **k** points around the minimum of each valley to resolve the relaxation times. Convergence with respect to all parameters was carefully tested. The converged *e*-ph calculations shown in this work require computing ~10 trillion *e*-ph matrix elements; these matrix elements are used on the fly to compute the *e*-ph self-energy, because their storage would require tens of terabytes of memory.

To reproduce the semiempirical calculations in ref. 13, we set the square modulus of the matrix elements to $\left|g^{\lambda,\mathbf{q}}_{n,m,\mathbf{k}}\right|^2 = [\hbar/(2M\omega_{\lambda,\mathbf{q}})]\cdot\Delta^2_\lambda(q)\cdot I^2(q)$, where $\Delta_\lambda(q)$ is the deformation potential for the phonon mode λ, and the overlap integral is computed in the rigid ion approximation (27), yielding $I(x) = 3[x\ cos(x) - sin(x)]/x^3$, where $x = q\ r_0$ and r_0 is the Wigner–Seitz cell radius (27). The deformation potentials are taken from ref. 13. (*i*) For optical phonons, $\Delta_{OP}(q) = b\cdot q$, where b = 5.0 eV for electron energy above 0.3 eV and b = 7.0 eV for electron energy below 0.3 eV. (*ii*) For acoustic phonons, $\Delta_{AC}(q) = a$, where $a = 2.1\cdot10^8$ eV/cm for electron energy above 0.3 eV and a = 0 eV for electron energy below 0.3 eV. (*iii*) For LO phonons, we add the Fröhlich contribution $\Delta^2_{LO,F} = [\hbar/(2M\omega_{\lambda,\mathbf{q}})]^{-1}\cdot[\pi e^2\hbar\omega_{LO}/(V_{uc}\ q^2)]\cdot(1/\epsilon_\infty - 1/\epsilon_0)$, where $\hbar\omega_{LO}$ is the LO phonon energy at the BZ center, V_{uc} is the volume of the unit cell, and ϵ_∞ and ϵ_0 are the high and low frequency dielectric constants of GaAs, respectively. All electron energies above are referenced to the CBM.

II Calculations. We carry out full-frequency *GW* calculations (16, 24) using the Berkeley *GW* code (37) to compute the imaginary part of the *GW* self-energy, $\mathrm{Im}(\Sigma^{GW}_{n,\mathbf{k}})$, and the associated II scattering rate $I^{II}_{n,\mathbf{k}} = (2/\hbar)\cdot[\mathrm{Im}(\Sigma^{GW}_{n,\mathbf{k}})]$. Here, $\mathrm{Im}(\Sigma^{GW}_{n,\mathbf{k}})$ denotes the diagonal matrix element of the imaginary part of the *GW* self-energy for the Kohn–Sham state $|n,\mathbf{k}\rangle$, and we compute $\mathrm{Im}(\Sigma^{GW}_{n,\mathbf{k}})$ on shell (i.e., we evaluate it at the LDA eigenvalues). Kinetic energy cutoffs of 10 and 45 Ry are used for the screened and bare Coulomb interactions, respectively, and 70 empty bands are used to compute the dielectric screening and the Green's function. For the *GW* calculations, the PARATEC code was used for the ground-state DFT LDA calculation, and we used the one-shot G_0W_0 approximation. Although a fine sampling of the BZ is essential to converge the *e*-ph self-energy, we find that an $8\times8\times8$ **k**-point grid is sufficient to converge the imaginary part of the *GW* self-energy. The data shown here are obtained with a Ga pseudopotential with the *d* states in the core. We have verified that including the semicore *d* states of Ga as valence states does not lead to significant changes in the II rates, which validates our approach, because only the imaginary part of the *GW* self-energy is of interest here. Details of the implementation of the imaginary part of the *GW* self-energy in our code can be found in refs. 37 and 38.

ACKNOWLEDGMENTS. This research was supported by the Scientific Discovery through Advanced Computing (SciDAC) Program on Excited State Phenomena in Energy Materials funded by US Department of Energy, Offices of Basic Energy Sciences and Advanced Scientific Computing Research Contract DE-AC02-05CH11231 at Lawrence Berkeley National Laboratory, which provided for algorithm and code developments and simulations, and National Science Foundation Grant DMR 10-1006184, which provided for basic theory and formalism. Work at the Molecular Foundry was supported by the Office of Science, Office of Basic Energy Sciences, US Department of Energy Contract DE-AC02-05CH11231. This research used resources of the National Energy Research Scientific Computing Center, which is supported by the Office of Science, US Department of Energy.

1. Fischetti M, Laux S (1996) Monte Carlo simulation of electron transport in Si: The first 20 years (IEEE). *Proceedings of the 26th European Solid State Device Research Conference*, eds Baccarani G, Rudan M (Editions Frontieres, Gif-sur-Yvette, France), pp 813–820.
2. Freitag M, et al. (2004) Hot carrier electroluminescence from a single carbon nanotube. *Nano Lett* 4(6):1063–1066.
3. Gabor NM, et al. (2011) Hot carrier-assisted intrinsic photoresponse in graphene. *Science* 334(6056):648–652.
4. Iveland J, Martinelli L, Peretti J, Speck JS, Weisbuch C (2013) Direct measurement of Auger electrons emitted from a semiconductor light-emitting diode under electrical injection: Identification of the dominant mechanism for efficiency droop. *Phys Rev Lett* 110(17):177406.
5. Tisdale WA, et al. (2010) Hot-electron transfer from semiconductor nanocrystals. *Science* 328(5985):1543–1547.
6. Polman A, Atwater HA (2012) Photonic design principles for ultrahigh-efficiency photovoltaics. *Nat Mater* 11(3):174–177.
7. Conibeer G, et al. (2009) Progress on hot carrier cells. *Sol Energy Mater Sol Cells* 93(6-7):713–719.
8. Chalabi H, Brongersma ML (2013) Plasmonics: Harvest season for hot electrons. *Nat Nanotechnol* 8(4):229–230.
9. Mukherjee S, et al. (2013) Hot electrons do the impossible: Plasmon-induced dissociation of H2 on Au. *Nano Lett* 13(1):240–247.
10. Gunn JB (1963) Microwave oscillations of current in III–V seminconductors. *Solid State Commun* 1(4):88–91.
11. Takeda E, Suzuki N (1983) An empirical model for device degradation due to hot-carrier injection. *Electron Devices Lett IEEE* 4(4):111–113.
12. Shah J (1999) *Ultrafast Spectroscopy of Semiconductors and Semiconductor Nanostructures* (Springer, Berlin), Vol 115.
13. Fischetti MV, Laux SE (1988) Monte Carlo analysis of electron transport in small semiconductor devices including band-structure and space-charge effects. *Phys Rev B Condens Matter* 38(14):9721–9745.
14. Jacoboni C, Reggiani L (1983) The Monte Carlo method for the solution of charge transport in semiconductors with applications to covalent materials. *Rev Mod Phys* 55(3):645–705.
15. Martin RM (2008) *Electronic Structrure: Basic Theory and Practial Methods* (Cambridge Univ Press, Cambridge, United Kingdom).
16. Hybertsen MS, Louie SG (1986) Electron correlation in semiconductors and insulators: Band gaps and quasiparticle energies. *Phys Rev B Condens Matter* 34(8):5390–5413.
17. Madelung O (1996) *Semiconductors—Basic Data* (Springer, Berlin).
18. Elsaesser T, Shah J, Rota L, Lugli P (1991) Initial thermalization of photoexcited carriers in GaAs studied by femtosecond luminescence spectroscopy. *Phys Rev Lett* 66(13):1757–1760.
19. Schoenlein R, Lin W, Ippen E, Fujimoto J (1987) Femtosecond hot-carrier energy relaxation in GaAs. *Appl Phys Lett* 51(18):1442–1444.
20. Shah J, et al. (1987) Determination of intervalley scattering rates in GaAs by subpicosecond luminescence spectroscopy. *Phys Rev Lett* 59(19):2222–2225.
21. Young JF, Gong T, Fauchet PM, Kelly PJ (1994) Carrier-carrier scattering rates within nonequilibrium optically injected semiconductor plasmas. *Phys Rev B Condens Matter* 50(4):2208–2215.
22. Baroni S, de Gironcoli S, Dal Corso A, Giannozzi P (2001) Phonons and related crystal properties from density-functional perturbation theory. *Rev Mod Phys* 73(2):515–562.
23. Giustino F, Cohen ML, Louie SG (2007) Electron-phonon interaction using Wannier functions. *Phys Rev B* 76:165108.
24. Hedin L (1965) New method for calculating the one-particle Green's function with application to the electron-gas problem. *Phys Rev* 139(3A):A796–A823.
25. Fröhlich H (1954) Electrons in lattice fields. *Adv Phys* 3(11):325–361.
26. Mahan GD (2010) *Condensed Matter in a Nutshell* (Princeton Univ Press, Princeton).
27. Ziman J (1961) *Electrons and Phonons* (Oxford Univ Press, London).
28. Noffsinger J, et al. (2010) EPW: A program for calculating the electron–phonon coupling using maximally localized Wannier functions. *Comput Phys Commun* 181(12):2140–2148.
29. Picozzi S, Asahi R, Geller C, Continenza A, Freeman AJ (2002) Impact ionization in GaAs: A screened exchange density-functional approach. *Phys Rev B Condens Matter Mater Phys* 65(11):113206.
30. Jung H, Taniguchi K, Hamaguchi C (1996) Impact ionization model for full band Monte Carlo simulation in GaAs. *J Appl Phys* 79(5):2473–2480.
31. Steiauf D, Kioupakis E, Van de Walle CG (2014) Auger recombination in GaAs from first principles. *ACS Photonics* 1(8):643–646.
32. Kadanoff LP, Baym G (1962) *Quantum Statistical Mechanics: Green's Function Methods in Equilibrium and Nonequilibrium Problems* (Benjamin, New York).
33. Ceperley DM, Alder BJ (1980) Ground state of the electron gas by a stochastic method. *Phys Rev Lett* 45(7):566–569.
34. Perdew JP, Zunger A (1981) Self-interaction correction to density-functional approximations for many-electron systems. *Phys Rev B Condens Matter Mater Phys* 23(10): 5048–5079.
35. Giannozzi P, et al. (2009) QUANTUM ESPRESSO: A modular and open-source software project for quantum simulations of materials. *J Phys Condens Matter* 21(39):395502.
36. Troullier N, Martins JL (1991) Efficient pseudopotentials for plane-wave calculations. *Phys Rev B Condens Matter* 43(3):1993–2006.
37. Deslippe J, et al. (2012) BerkeleyGW: A massively parallel computer package for the calculation of the quasiparticle and optical properties of materials and nanostructures. *Comput Phys Commun* 183(6):1269–1289.
38. Spataru CD (2004) Electron excitations in solids and novel materials. PhD thesis (University of California, Berkeley, CA).